Rare Met.
https://doi.org/10.1007/s12598-024-02850-2

RARE METALS

ORIGINAL ARTICLE

Circumventing brittleness of 3D-printed Al_2O_3 cellular ceramic structures via compositing with polyurea

Xue-Qin Zhang, Ru-Yue Su, Xiong Gao, Jing-Yi Chen, Guo Liu*, Ru-Jie He*, Ying Li

Received: 25 December 2023 / Revised: 23 February 2024 / Accepted: 23 March 2024

Abstract Benefiting from excellent mechanical properties and low density, cellular ceramic structures (CCSs) are competitive candidates as structural components. However, inherent brittleness from strong chemical bonds among atoms extremely impeded CCSs' application. Natural materials occupied outstanding strength and toughness simultaneously due to the dual-phase interpenetrated structure. Inspired by natural materials, it was proposed to fabricate coating covered and fulfilled polyurea/CCS interpenetrated composites (C/CCSs and B/CCSs) to circumvent the brittleness of 3D-printed Al_2O_3 CCSs. It was demonstrated that polyurea coating had less effect on the compressive strength of C/CCSs but tremendously improved their energy-absorbing ability. The energy-absorbing ability of C/CCSs was improved from 26.48–52.57 kJ·m^{-3} of CCSs to 1.04–1.89 MJ·m^{-3} because of the extended plateau stage. Furthermore, compressive strength and energy-absorbing ability of B/CCSs were strengthened to 1.33–1.36 and 2.84–4.61 times of C/CCSs, respectively. Besides, failure mode of C/CCSs changed from localized deformation to fracturing entirely with the increase in relative density of CCSs inside, which was the same as that of CCSs. However, with the help of polyurea coating, C/CCSs were still intact at strains up to 60%, which would never fail catastrophically as CCSs at low strains. B/CCSs tended to fracture as a whole, which was not influenced by relative density of pristine CCSs. It was believed that this work provided a creative way to circumvent the brittleness of CCSs and improve their mechanical performances.

Keywords Cellular ceramic structures; Dual-phase interpenetrated composites; Energy-absorbing ability; Compressive strength; 3D printing

1 Introduction

Cellular ceramic structures (CCSs) were more and more prominent in engineering due to their low density and superior performance in strength and stiffness [1–4]. However, CCSs were also known for their unexpected brittleness. High brittleness from strong chemical bonds among atoms always caused sudden destruction of ceramic components [5–7]. Poor toughness of CCSs significantly threatened life and property security. Hence, circumventing the disadvantaging effect of CCSs' brittleness was thus in great demand.

It was concluded that the brittleness of CCSs could be alleviated by materials and structures, i.e., toughened ceramic materials and optimized structures of CCSs [8–10]. Liu et al. [8] prepared zirconia-toughened alumina ceramics via stereolithography apparatus. The addition of zirconia was 15 vol%. It was proved that toughness of zirconia-toughened alumina ceramics was improved to 4.05 MPa·m$^{1/2}$. Zhang et al. [10] introduced ZrO_2(3Y) as the second phase in Al_2O_3 to fabricate hollow CCSs with body-centered cubic (BCC) structure by vat photopolymerization. The addition of ZrO_2(3Y) was 6 wt%. It was proved that ZrO_2(3Y) significantly improved the damage tolerance of Al_2O_3. The toughness of ZrO_2(3Y)/Al_2O_3

X.-Q. Zhang, R.-Y. Su, X. Gao, J.-Y. Chen, R.-J. He*, Y. Li
Institute of Advanced Structure Technology, Beijing Institute of Technology, Beijing 100081, China
e-mail: herujie@bit.edu.cn

G. Liu*
Department of Mechanical Engineering, City University of Hong Kong, Hong Kong 999077, China
e-mail: guoliu3@cityu.edu.hk

Published online: 28 June 2024

hollow CCS reached 6.64 MPa·m$^{1/2}$. Except for optimized constituents, novel structures were adopted to improve the damage-tolerant ability of CCSs. Al_2O_3 CCSs with a structure of graded diamond-type surface were designed and prepared by lithography-based three-dimensional (3D) printing technology. It possessed load-bearing capacity at strain of 50% and exhibited a pseudo-ductile failure mode rather than fracture suddenly [9]. Furthermore, the characteristic chambered "wall-septa" microstructure in cuttlebone inspired researchers to propose an optimal waviness gradient in CCSs. It was proved that CCSs with "wall-septa" microstructure occupied high specific stiffness (8.4 MN·m·kg^{-1}) and energy absorption (4.4 kJ·kg^{-1}) simultaneously [11]. However, optimized constituents and structures did not exhibit the expected level of performance. Ceramic components still disintegrated under compression. The catastrophic damage resulting from the brittleness of ceramics was still a tackle and potential threat stopping CCSs from being reliable candidates for engineering.

Based on current research, it was upsetting but still a reality that we were powerless to overcome the brittleness and improve the toughness of ceramics via materials and structures. Hence, discovering a creative way to perfect the energy-absorbing ability without damaging load-bearing capacity is urgent and critical for CCSs. Luckily, strong and tough natural materials provided a new idea. As revealed by Ritchie [12] and Barthelat et al. [13], stiff but brittle materials were major constitutions of natural materials with remarkable toughness and strength. The key to outstanding strength and toughness of natural materials was another tough constitution. The hard phase in natural materials was covered by a tough phase, forming a dual-phase interpenetrated composite. The hard phase supported loading, providing superior strength. The soft phase, on the one hand, dispersed the accumulated stress to the whole structure. On the other hand, it kept the integrity of structures under loadings, avoiding the disintegration of fragments. As early as 2008, Munch et al. [14] mimicked the brick–mortar dual-phase interpenetrated structure in an abalone shell and combined Al_2O_3 and polymethyl methacrylate in an interpenetrated state. The toughness of the obtained dual-phase interpenetrated composite was more than 300 times that of its constituents. Conch shell with a cross-lamellar dual-phase interpenetrated structure exhibited around ten times higher toughness than widely explored nacre. Inspired by conch shell, Li et al. [15] fabricated the epoxy/Al_2O_3 interpenetrated composite. The flexural strength and fracture work of epoxy/Al_2O_3 interpenetrated composite reached as high as 165 MPa and 8.2 kJ·m^{-2} at the same time, achieving the trade-off between strength and toughness. In fact, the as-fabricated CCS was an air/CCS interpenetrated composite. However, the second phase here, i.e., air, was absolutely ineffective in load-bearing and damage tolerance. Hence, enlightened by natural materials, it would be a great idea to replace the air with tough materials to form a dual-phase interpenetrated composite.

Herein, a simple way is proposed to circumvent the brittleness of CCSs by emulating the dual-phase interpenetrated composites in natural materials. Al_2O_3 CCSs were fabricated by vat photopolymerization technology and pressureless sintering. Subsequently, Al_2O_3 CCSs were encapsulated with polyurea in two different ways, i.e., coating and fulfilled bulk, forming bioinspired coating covered and fulfilled polyurea/CCS interpenetrated composites (C/CCSs and B/CCSs). All CCSs, C/CCSs, and B/CCSs were examined under identical compressive loading to comparatively investigate how bioinspired dual-phase interpenetrated composites worked in circumventing the brittleness of CCSs. It was believed to be a simple and feasible approach to circumvent the disadvantageous effect of the brittleness of CCSs and reverse the poor application situation of CCSs.

2 Experimental

2.1 3D printing

Models of CCSs with a structural configuration of Schwarz P were generated by MSLattice software. CCSs were composed of unit cells with size of 6 mm × 6 mm × 6 mm in a 5 × 5 × 5 array. Relative densities of 20%, 30% and 40% were involved in this work. As illustrated in Fig. 1, green bodies of CCSs were fabricated by 3D printer from an Al_2O_3 photosensitive slurry. Then, debinding and sintering were executed on as-printed green bodies in muffle furnaces at 600 °C for 2 h and 1650 °C for 2 h. Details about 3D printing of CCSs were listed in previous work [16].

2.2 Infiltration

C/CCSs and B/CCSs were finally obtained after compositing CCSs and polyurea. As shown in Fig. 1, polyurea used in this work was obtained after mixing modified isocyanate prepolymer and 3,3′-dichloro-4,4′-diaminodiphenyl-methane at a weight ratio of 10:1.5. The mixture was poured onto the surface of CCSs, and the pressure was applied to get mixture infiltrated in CCSs. After that, polyurea fulfilled interpenetrated B/CCSs were obtained. To get coating covered C/CCSs, the redundant polyurea inside CCSs was blown with high-pressure flow. Subsequently, it was necessary to place as-composited B/CCSs and C/CCSs in an oven at 80 °C for 72 h, followed by

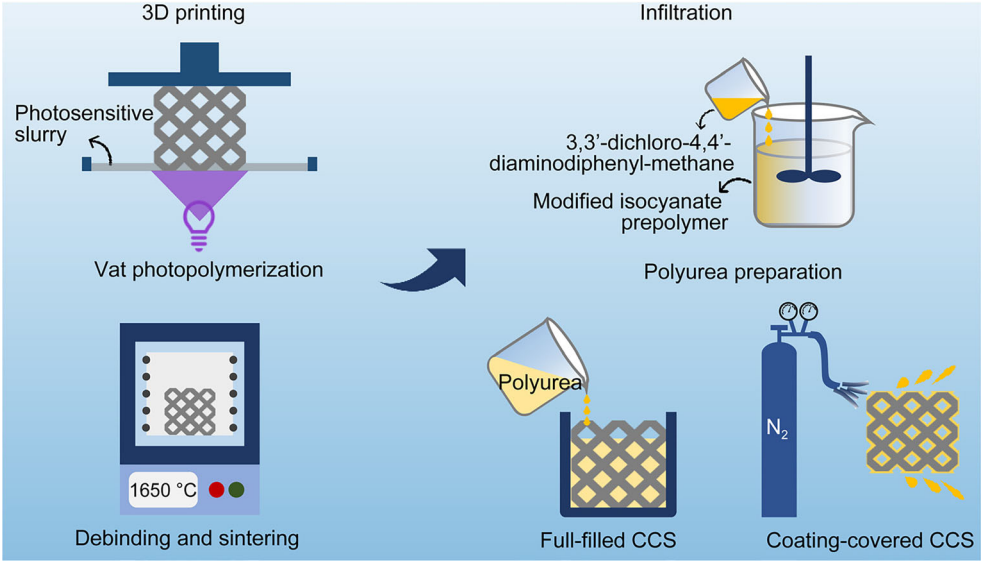

Fig. 1 Fabricating process of CCSs, C/CCSs and B/CCSs

another 72 h in a standard environment to ensure that the polyurea maintained its optimal state.

2.3 Characterization and examination

The digital micrometer and scale were used to measure the size and weight of components, respectively. Besides, an EVO18 scanning electron microscopy from Zeiss and a digital microscope from Dino-Lite were used to observe micro morphologies of CCSs. An LD23 universal testing machine from Labsans was used to examine the mechanical properties of CCSs, C/CCSs, and B/CCSs under compressive loading. Three samples were repeatedly tested under compression. The loading speed was set as 1 mm·min^{-1}. The bonding strength of polyurea and additively manufactured ceramic was also tested by tensile testing. The loading speed was 0.2 mm·min^{-1}. A pair of Teflon films were placed between the CCSs and pressure heads to decrease the influence of friction. The deformation process of components was captured with a camera.

3 Results and discussion

3.1 Morphologies of structures

A triply periodic minimal surface (TPMS) structure named Schwarz P was adopted in this work to investigate how polyurea worked in circumventing the brittleness of CCSs. Figure 2a–c displays morphologies of CCSs with relative densities of 20%, 30%, and 40%. It was found that CCSs with a structure of Schwarz P were accurately fabricated, which was almost the same as designed models on a macro scale. Walls of Schwarz P CCSs got thicker and thicker as relative density increased from 20% to 40%. Table 1 lists structural parameters of CCSs, C/CCSs, and B/CCSs. Components were named based on their states and relative density. For example, CCS20 represented CCS with a relative density of 20%. As listed in Table 1, there was a ~ 20% deviation between sizes of as-designed models and final products of CCSs. Because photosensitive polymers, acting as a binder to connect ceramic powders, took a volumetric fraction of 50% in slurry. In debinding process, cured polymers were burned and expelled from green bodies of CCSs, leaving pores accounting for a volume fraction of 50%. Loose ceramic powders got densification in subsequent sintering, leading to the volume shrinkage. Besides, apparent step-wise morphologies could be observed on the surface of CCSs with scanning electron microscopy. Step-wise morphologies were ascribed to the layer-by-layer forming characteristic of vat photopolymerization.

CCS, C/CCS and B/CCS with a relative density of 40% are displayed in Fig. 2d–f. According to the top and side views of C/CCS40, we found that C/CCS40 looked shining after covering a transparent polyurea coating. As listed in Table 1, C/CCSs were bigger and occupied higher density as CCSs because of attached polyurea coatings. Pristine CCS40 inside B/CCS40 was fully stuffed by polyurea. Similarly, B/CCSs were higher in density than both CCSs and C/CCSs because of fulfilled polyurea. Besides, polyurea and CCSs were bound tightly. The binding strength of polyurea and coarse surface of CCSs was (3.97 ± 0.20) MPa.

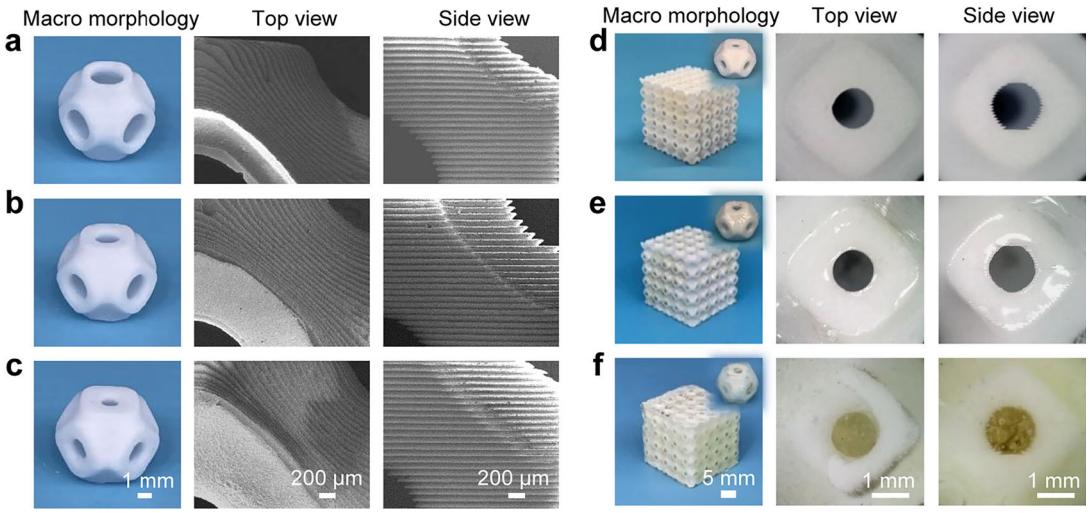

Fig. 2 Morphologies of **a** CCS20, **b** CCS30, **c** CCS40, **d** CCS40, **e** C/CCS40 and **f** B/CCS40

Table 1 Structural parameters of CCSs, C/CCSs and B/CCSs

No.	Length / mm	Width / mm	Height / mm	Mass / g	Apparent density / ($g \cdot cm^{-3}$)
CCS20	24.11 ± 0.20	24.02 ± 0.16	22.47 ± 0.27	10.05 ± 0.17	0.77 ± 0.01
CCS30	24.10 ± 0.21	23.73 ± 0.40	22.82 ± 0.23	14.93 ± 0.76	1.14 ± 0.04
CCS40	24.17 ± 0.13	24.14 ± 0.16	22.93 ± 0.41	19.97 ± 0.12	1.49 ± 0.03
C/CCS20	24.19 ± 0.27	24.13 ± 0.14	22.51 ± 0.16	13.00 ± 0.61	0.99 ± 0.05
C/CCS30	24.52 ± 0.43	24.42 ± 0.40	23.27 ± 0.51	18.28 ± 1.16	1.31 ± 0.02
C/CCS40	24.82 ± 0.30	24.56 ± 0.12	23.46 ± 0.23	24.63 ± 0.20	1.72 ± 0.03
B/CCS20	24.42 ± 0.21	24.18 ± 0.17	22.65 ± 0.37	20.42 ± 0.51	1.60 ± 0.01
B/CCS30	24.35 ± 0.40	24.24 ± 0.39	23.26 ± 0.20	24.49 ± 0.75	1.85 ± 0.09
B/CCS40	24.50 ± 0.28	24.40 ± 0.20	23.08 ± 0.41	27.72 ± 1.12	2.07 ± 0.05

3.2 Mechanical properties of CCSs

Responses of CCSs under compressive loading were examined in the first place. The stress–strain curves and final states of Schwarz P CCSs with relative densities of 20%, 30% and 40% are displayed in Fig. 3. It is concluded from Fig. 3a that no matter what relative density was, the loading CCSs suffered increased linearly as the increase in deformation at initial. As compression went on, stress–strain curves descended slightly and rebounded before decreasing dramatically. The first decrease was caused by the partial fracture of CCSs. Because the stress in some regions exceeded the strength of 3D-printed Al_2O_3 ceramics. Luckily, remained structures were capable of shouldering loading. So, stress–strain curves would bounce and raise again until structures fractured, losing load-bearing capacity completely. As CCSs were destroyed, stress–strain curves decreased dramatically, which was the typical failure characteristic of ceramic components. Besides, stress–strain curves of CCSs moved upwards as

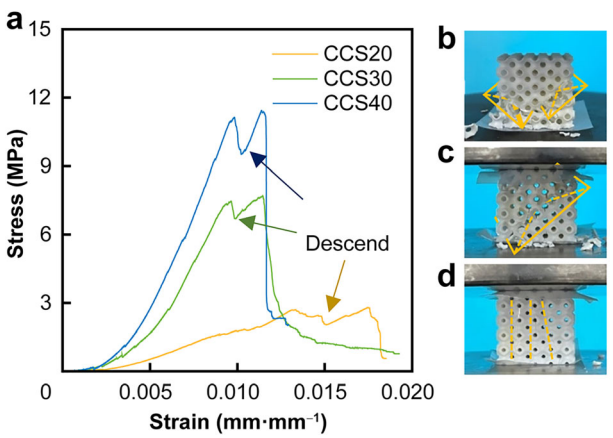

Fig. 3 Responses of CCSs under compressive loading: **a** representative stress–strain curves; final states of **b** CCS20, **c** CCS30 and **d** CCS40

the increase in relative density. The max value in stress–strain curve was defined as the compressive strength of CCSs. That was to say, the compressive strength of CCS40

((11.79 ± 1.65) MPa) was higher than that of CCS30 ((6.65 ± 1.41) MPa). The compressive strength of CCS20 ((3.33 ± 0.66) MPa) was the lowest. The higher the relative density was, the thicker the walls of CCSs were. Thickened walls were capable of withstanding higher loading, which had been extensively reported [17, 18]. However, due to limited strains, CCS20, CCS30, and CCS40 only dissipated (26.48 ± 2.43), (30.50 ± 7.57) and (52.57 ± 3.37) $kJ \cdot m^{-3}$, respectively.

Final states of CCSs, as shown in Fig. 3b–d, proved the brittleness of CCSs again. Cellular metal structures (CMSs) and cellular polymer structures (CPSs) were always compressed tightly to a large deformation of 30% [19–22]. However, CCSs cracked and lost load-bearing capacity at a strain of less than 0.02. Catastrophic destruction happened once loading exceeded the strength of CCSs. That was why the brittleness of CCSs tremendously hindered their application. Furthermore, relative density had an influence on the failure mode of Schwarz P CCSs. As labeled in Fig. 3b, Schwarz P CCS20 deformed localized. Walls of CCS20 cracked along planes with a 45° to the horizontal plane, which was the same as the failure mode of lattice-based CCSs [16]. With the increase in relative density, the failure mode of Schwarz P CCSs shifted from localized deformation to fractured entirely because of the increased stiffness, which was also proved before [23].

3.3 Response of polyurea/CCS interpenetrated composites with a relative density of 20%

The urgency to decrease the adverse influence of brittleness was arose by the response of CCSs under compressive loading. Drawing inspiration from dual-phase interpenetrated natural materials, the fabrication of polyurea/CCS interpenetrated composites was proposed, with the aim of optimizing mechanical properties of CCSs.

The Schwarz P CCSs with a relative density of 20% were first covered by polyurea, forming coating covered C/CCS20 and fulfilled B/CCS20, respectively. Stress–strain curves of CCS20, C/CCS20, and B/CCS20 under compressive loading are shown in Fig. 4a. It is surprised that sudden fracture did not happen in C/CCS20 and B/CCS20 at a low strain. The compression of polyurea/CCS interpenetrated composites went through the linear elastic stage, plateau stage and densification stage in succession [24, 25].

At the initial test, the stress in C/CCS20 and B/CCS20 suffered increased linearly with the increase in strain, which was the same as that of CCSs. This stage was named as linear elastic stage based on the linear relationship between stress and strain. It should be noticed that the elastic mentioned here was tremendously different from the recoverable elastic deformation, which was defined only based on the morphology of stress–strain curves [24]. Unrecoverable fractures still happened on C/CCS20 and B/CCS20 in the linear elastic stage. The linear elastic stage terminated at the first peak of stress–strain curves. Peak value was defined as the compressive strength of dual-phase interpenetrated composites [25]. As shown in Fig. 4b, compressive strength of CCS20, C/CCS20, and B/CCS20 were (3.33 ± 0.66), (3.85 ± 0.52) and (5.22 ± 0.54) MPa, respectively. Compressive strength of C/CCS20 and B/CCS20 distributed on a larger range. Because ceramics were flaw-sensitive, their mechanical properties were easily influenced by flaws. Besides, the compressive strength of C/CCS20 was slightly higher than CCS20, meaning polyurea coating was too thin to provide additional load-bearing capacity. There was a 57% improvement in the compressive strength of B/CCS20 when CCS20 was fulfilled with polyurea. It was hard for walls of CCS20 to deform after constrained by polyurea network. CCS20 could adjust position only after stretching or compressing polyurea. So, B/CCS20 was capable of withstanding higher loading. When stress climbed to the peak, pristine CCSs inside C/CCS20 and B/CCS20 were largely destroyed and lost the most load-bearing capacity. Luckily, the polyurea network avoided the collapse of fragments of pristine CCSs. It should be mentioned that strains of C/CCS20 and B/CCS20 at the end of linear elastic stage (1.66% ± 0.35% and 1.95% ± 0.37%) were limited. There was no room for broken fragments to adjust positions. So, as seen in Fig. 5, no crack could be observed on C/CCS20 and B/CCS20 at the end of linear elastic stage.

As stress went across the peak, compression stepped into plateau stage. Plateau stage started from the end of linear elastic stage, and terminated at the strain corresponding to the max energy-absorbing efficiency. The energy-absorbing efficiency was a ratio of the energy absorbed per unit volume at a given strain to the energy absorbed per unit volume by an ideal energy absorber up to the same strain. There was an obvious drop in the load-bearing capacity of C/CCS20 at the initial plateau stage. But it was not catastrophic. Load-bearing capacity of C/CCS20 declined slowly after first quick fall. It would go upwards again after a slow and long decrease. There was a sort of difference between stress–strain curves of B/CCS20 and C/CCS20 in plateau stage. At initial plateau stage, there was just a slight decrease in the stress–strain curve of B/CCS20. Then, stress–strain curve of B/CCS20 slowly upward, rather than decreasing. Besides, there were significant differences between states of C/CCS20 and B/CCS20 at plateau stage. As exhibited in Fig. 5c, when strain reached 0.04, pristine CCS of C/CCS20 cracked in three modes: horizontal fracture, vertical fracture, and inclined fracture. Inclined fracture took the largest

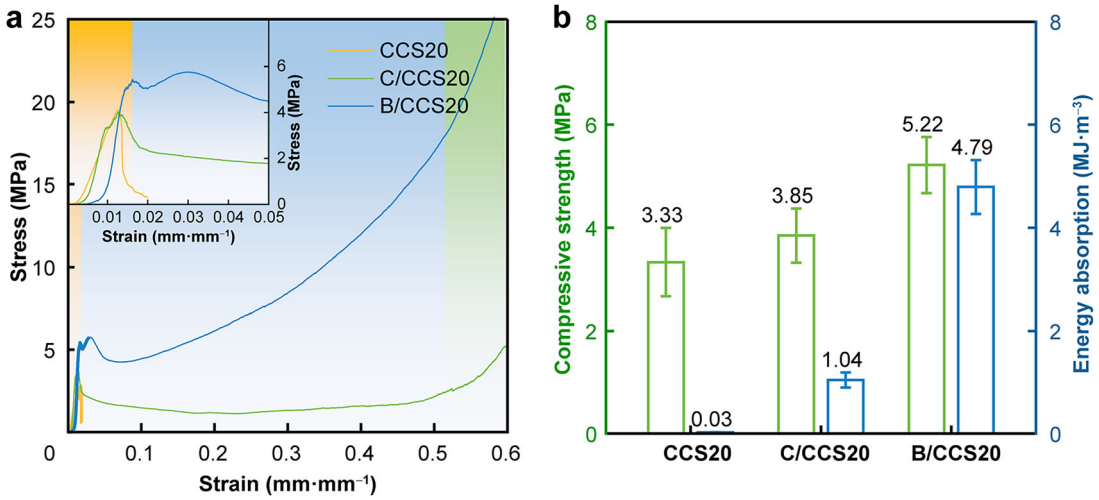

Fig. 4 **a** Representative stress–strain curves and **b** compressive strength and energy absorption of CCS20, C/CCS20 and B/CCS20, where yellow, blue and green areas represent linear elastic stage, plateau stage and densification stage of B/CCS20, respectively

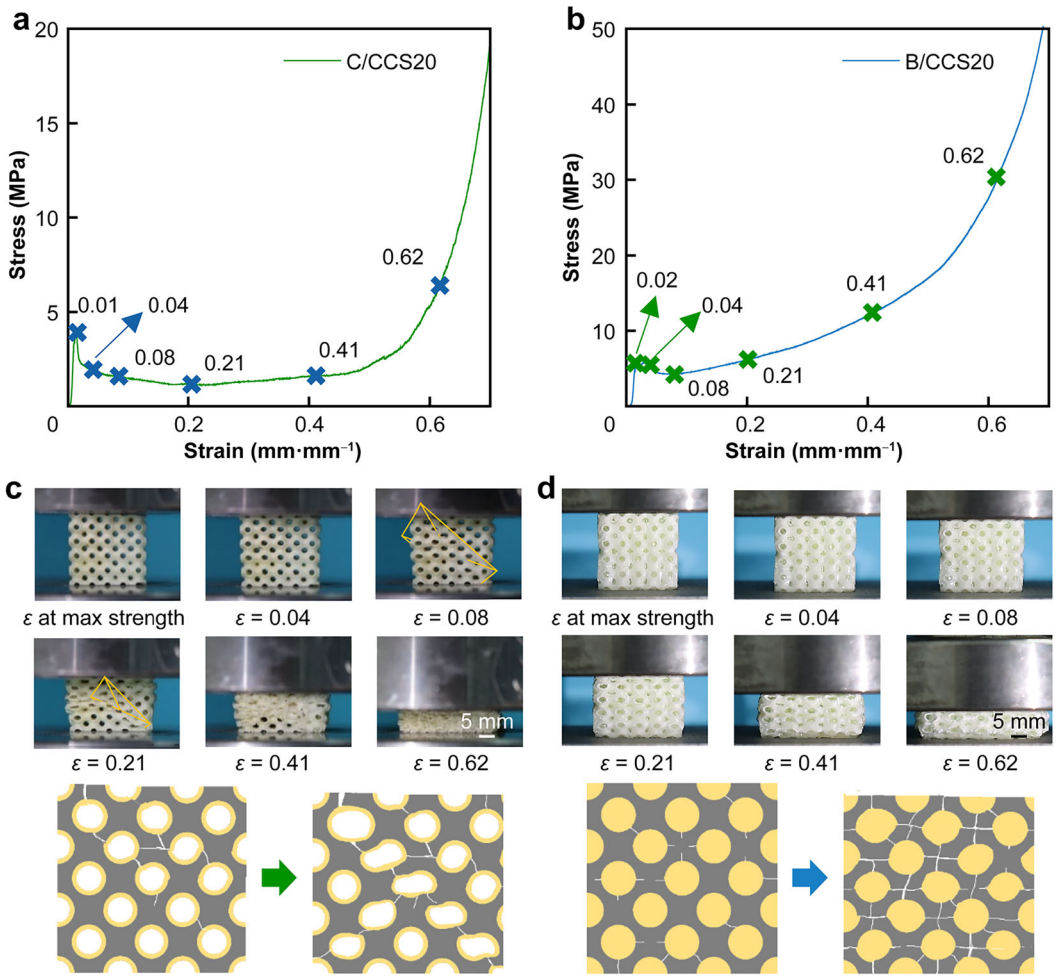

Fig. 5 **a**, **b** Compressive stress–strain curves and **c**, **d** deformation processes of C/CCS20 and B/CCS20

proportion. Most fractures concentrated on a plane whose angle to horizontal plane was ~ 45°. Such localized deformation was more and more obvious under larger compression. However, localized deformation did not happen on B/CCS20. As shown in Fig. 5d, pristine CCS in B/CCS20 fractured horizontally and vertically. B/CCS20 deformed homogeneously. The distinction between deformation modes of C/CCS20 and B/CCS20 was attributed to proportions of polyurea. Only a thin polyurea coating maintained the structural integrity of C/CCS20. Localized deformation still happened on C/CCS20 like that happened on CCS20 and cellular structures prepared from tough materials [26–29]. However, polyurea in B/CCS20 took a larger volumetric proportion than that in C/CCS20, which improved the homogeneity of B/CCS20 and weakened the effect of flaws. So, B/CCS20 deformed evenly under compressive loading.

Furthermore, energy-absorbing ability, i.e., the energy dual-phase interpenetrated composites consumed per cubic meter in linear elastic stage and plateau stage, was a significant parameter to measure the effect of polyurea in circumventing the brittleness of ceramics. It is statically concluded in Fig. 4b that CCS20 dissipated 26.48 ± 2.43 $kJ{\cdot}m^{-3}$ before collapsing. Coupled with polyurea coating, C/CCS20 was capable of absorbing 1.04 ± 0.15 $MJ{\cdot}m^{-3}$ under compression, 39 times that of CCS20. The attractive improvement in energy-absorbing ability of C/CCS20 was ascribed to the interface debonding of polyurea and pristine CCSs, compression of polyurea, and crush of pristine CCSs. Furthermore, B/CCS20 was preferable to C/CCS20 in energy-absorbing ability. B/CCS20 could consume 4.79 ± 0.52 $MJ{\cdot}m^{-3}$ in compression, which was even 4.6 times that of C/CCS20. Because fulfilled polyurea provided additional support to maintain the position of fragments of pristine CCS inside B/CCS20. To achieve the same deformation, fragments were crushed severely at contacting positions. So, B/CCS20 consumed much more energy than C/CCS20. Attractive energy consumption ability powerfully proved that introducing a soft phase to form a dual-phase interpenetrated composite was undoubtedly a reliable way to settle the adverse effect of CCSs' brittleness.

When deformation reached the strain corresponding to maximum energy-absorbing efficiency, compression entered the densification stage. In this stage, the stress dramatically increased as the increased deformation. Because broken walls in C/CCS20 and B/CCS20 were forced to connect with others due to the narrower space between pressure heads, making mechanical properties of C/CCS20 and B/CCS20 closer to that of Al_2O_3 bulk. So, polyurea/CCS interpenetrated composites were able to shoulder more and more loading.

3.4 Response of polyurea/CCS interpenetrated composites with relative densities of 30% and 40%

CCSs with relative densities of 30% and 40% were also covered with polyurea to comparatively examine the mechanical properties of polyurea/CCS interpenetrated composites. Figure 6a, c displayed stress–strain curves of CCS30, C/CCS30, B/CCS30, and CCS40, C/CCS40, B/CCS40 under compressive loading. It was revealed that compressions of C/CCS30, C/CCS40, B/CCS30, and B/CCS40 went through linear elastic stage, plateau stage, and densification, which were identical to those of C/CCS20 and B/CCS20. Besides, as shown in Fig. 6b, d, compressive strength of C/CCS30 ((7.22 ± 0.37) MPa) and C/CCS40 ((11.13 ± 2.44) MPa) was approximately equivalent to that of CCS30 ((6.65 ± 1.41) MPa) and CCS40 ((11.79 ± 1.65) MPa). It proved that polyurea coating made no difference in strengthening CCSs. Furthermore, stress–strain curves of polyurea fulfilled CCS also topped that of coating covered CCS. Hence, the compressive strength of B/CCS30 and B/CCS40 reached (9.68 ± 1.19) and (14.79 ± 0.83) MPa, almost 1.34 and 1.33 times of coating covered C/CCS30 and C/CCS40, respectively.

Except for compressive strength, energy-absorbing ability of polyurea/CCS interpenetrated composites was also comparatively discussed here. As concluded in Fig. 6, C/CCS30, B/CCS30, C/CCS40, and B/CCS40 were capable of dissipating energy of (1.71 ± 0.39), (4.86 ± 0.74), (1.89 ± 0.37) and (6.54 ± 0.94) $MJ{\cdot}m^{-3}$ in compressive process, which were 56, 159, 36 and 124 times of energy-absorbing ability of corresponding CCSs. The remarkable energy-absorbing ability of polyurea/CCS interpenetrated composites was ascribed to the extended plateau stage resulting from introduced polyurea [30, 31]. Furthermore, it is concluded from Figs. 4, 6 that energy-absorbing ability of polyurea fulfilled CCSs was tremendously higher than that of polyurea-coated CCSs. It was closely related to the strain at max energy-absorbing efficiency and plateau stress. It was extracted from stress–strain curves that strains of B/CCS20, B/CCS30, and B/CCS40 at max energy-absorbing efficiency (0.23 ± 0.01, 0.25 ± 0.03, 0.25 ± 0.02) were 0.50 ± 0.02, 0.52 ± 0.01, 0.50 ± 0.03, as displayed in Fig. 7a, slightly lower than strains of C/CCS20, C/CCS30, and C/CCS40 at max energy-absorbing efficiency (0.27 ± 0.03, 0.20 ± 0.02, 0.17 ± 0.01), i.e., 0.57 ± 0.03, 0.57 ± 0.01, 0.55 ± 0.02, respectively. Smaller strains meant that B/CCSs stepped into densification stage ahead of C/CCSs. B/CCSs ceased to consume energy at smaller deformation. However, as revealed in Fig. 7b, plateau stress of B/CCSs was

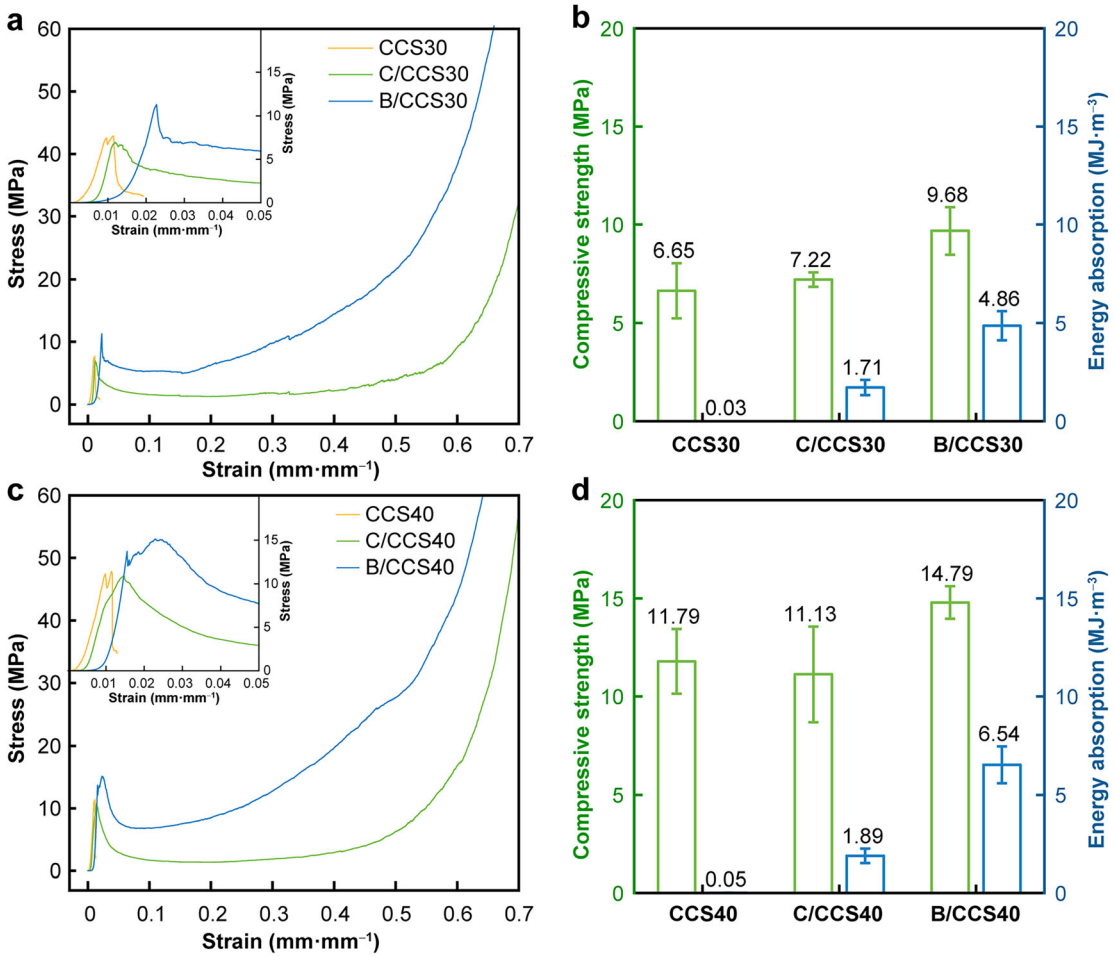

Fig. 6 Compressive stress–strain curves of **a** CCS30, C/CCS30, B/CCS30 and **c** CCS40, C/CCS40, B/CCS40; compressive strength and energy absorption of **b** CCS30, C/CCS30, B/CCS30 and **d** CCS40, C/CCS40, B/CCS40

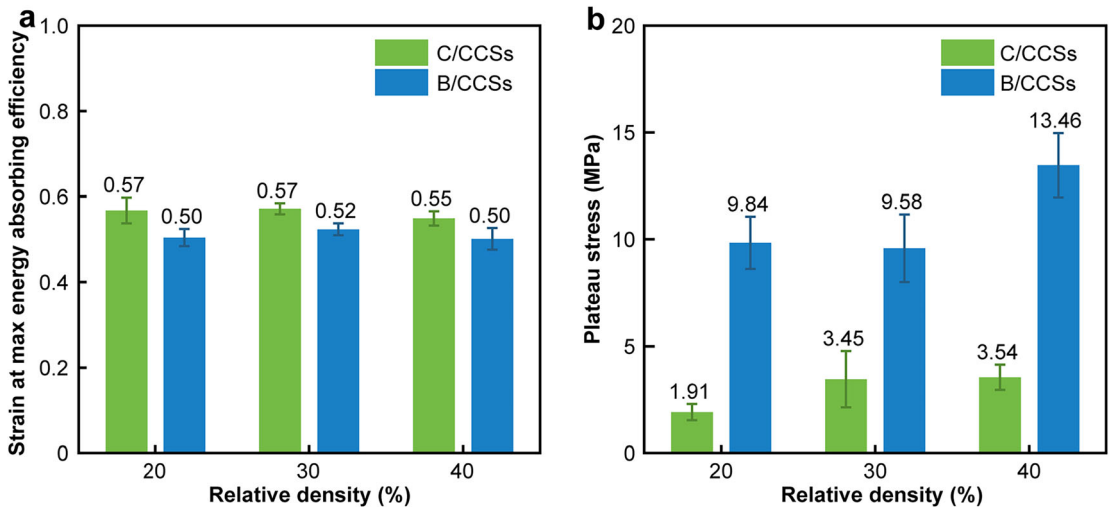

Fig. 7 **a** Strain at max energy-absorbing efficiency and **b** plateau stress of polyurea/CCS interpenetrated composites

tremendously higher than that of C/CCSs. Higher plateau stress meant energy B/CCSs dissipated per deformation was much higher than C/CCSs. With the comprehensive effect of plateau stress and strain at max energy-absorbing efficiency, B/CCSs presented a more attractive energy-absorbing ability.

Figure 8 discloses deformation processes of C/CCS30, B/CCS30, C/CCS40, and B/CCS40. Although pristine CCSs were already broken, no crack could be observed in polyurea/CCS interpenetrated composites at the end of the linear elastic stage due to less deformation. When compression stepped into plateau stage, fragments embodied in polyurea networks had to separate from each other. As polyurea expanded in the direction perpendicular to the loading direction, the embodied fragments had to move together, thus forming eye-catching cracks. It should be mentioned that broken fragments of pristine CCS inside C/CCS30 slipped along a 45° plane under compressive loading, which was the same as that of C/CCS20. However, no localized deformation could be observed in deformation process of C/CCS40. C/CCS40 tended to deform homogeneously. That was to say, the deformation mode of C/CCSs changed from localized deformation to homogeneous deformation with the increase in relative density [16, 18]. However, relative density of pristine CCSs inside B/CCSs did not change the deformation process of B/CCSs. When pristine CCSs were fulfilled with polyurea, B/CCSs always deformed evenly.

3.5 Specific mechanical properties of polyurea/CCS interpenetrated composites

There was no doubt that introduced polyurea perfected mechanical properties of CCSs. However, introduced polyurea increased densities of components, which might cause the loss of specific mechanical properties. In fact, both lightweight and mechanical properties were significant for structural components. Hence, it was vital to discuss specific mechanical properties of polyurea/CCS interpenetrated composites.

Figure 9 displays the specific mechanical properties of CCSs, C/CCSs, and B/CCSs. As concluded before, the load-bearing capacity of CCSs and C/CCSs was basically the same. Compressive strength of B/CCSs was much higher than those of CCSs and C/CCSs. Taking density into consideration, something different happened. Specific compressive strength of CCSs was higher than that of polyurea/CCS interpenetrated composites. For example, specific compressive strength of CCS20 was (4.33 ± 0.86) $N{\cdot}m{\cdot}g^{-1}$. Specific compressive strength of C/CCS20 and B/CCS20 was (3.89 ± 0.53) and (3.26 ± 0.34) $N{\cdot}m{\cdot}g^{-1}$, respectively. Because additional load-bearing capacity from polyurea was significantly weakened by the increased density. Luckily, polyurea/CCS interpenetrated composites possessed an absolute advantage in specific energy-absorbing ability. As disclosed in Fig. 9, specific energy absorption of B/CCSs and C/CCSs were 2.63–3.16 and

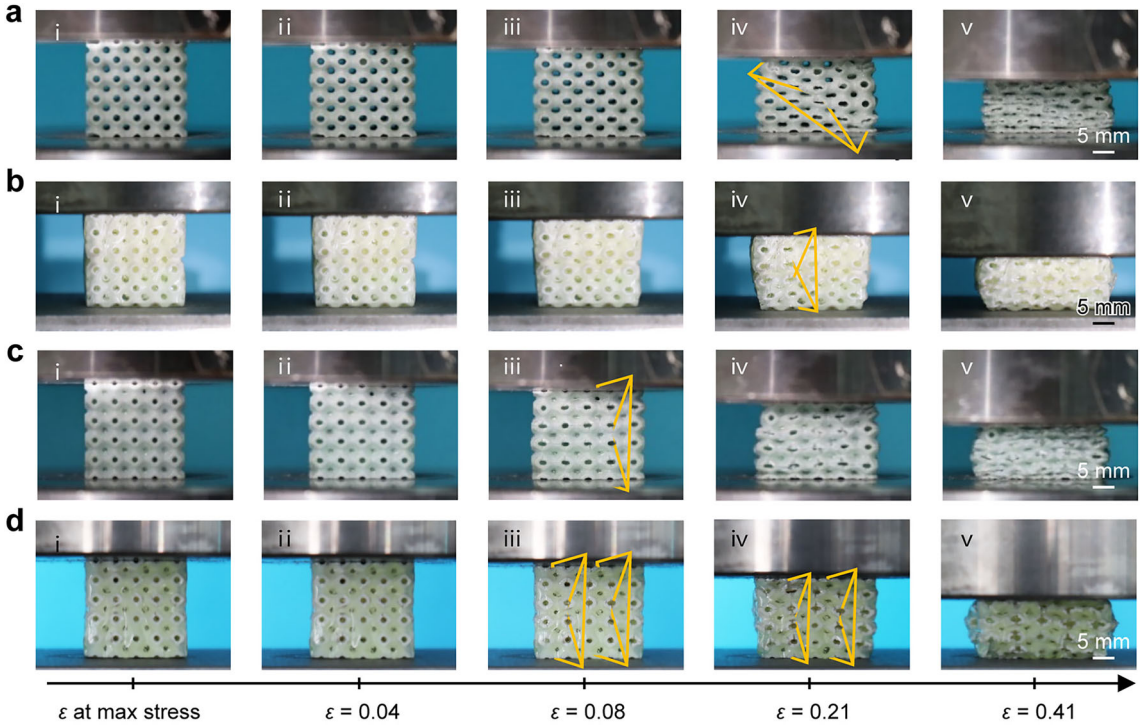

Fig. 8 Deformation processes of **a** C/CCS30, **b** B/CCS30, **c** C/CCS40 and **d** B/CCS40

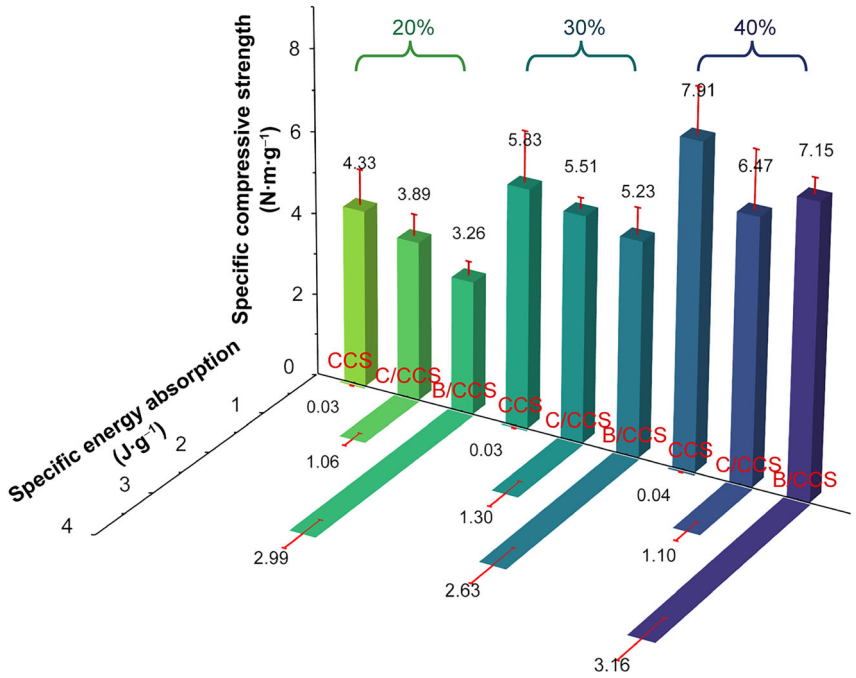

Fig. 9 Specific mechanical properties of CCSs, C/CCSs, and B/CCSs

1.06–1.30 $J \cdot g^{-1}$, tremendously higher than those of CCSs (0.03–0.04 $J \cdot g^{-1}$).

Figure 10 displays the Ashby map of specific energy absorption versus specific compressive strength of components. CCSs, CMSs and CPSs were involved in Fig. 10. It was clear that specific compressive strength of CCSs, CMSs, and CPSs were arranged in the same range. However, there was a tremendous difference in specific energy-absorbing ability of them. Specific energy absorption of CCSs was inferior to that of CMSs and CPSs due to tiny deformations, which was caused by high brittleness of ceramic materials [6, 16, 18, 32–34]. Specific energy absorption of CMSs was the most outstanding due to their high strength and excellent plasticity [35–39]. Although load-bearing capacity and energy-absorbing ability of CPSs were not as attractive as those of CMSs, low density was dominant. So, specific energy absorption of CPSs was also higher than that of CCSs [40–43]. According to calculated results, it can be found that specific energy absorption of Schwarz P CCSs in this work was plane like other CCSs. However, there was a remarkable enhancement in specific energy-absorbing ability of polyurea/CCS interpenetrated composites after compositing them with polyurea. Specific energy-dissipating ability of C/CCSs was 30–50 times that of CCSs. The energy B/CCSs consumed per gram was even 2–3 times that of C/CCSs. The specific energy absorption of polyurea/CCS interpenetrated composites not only exceeded CCS but also was on par with CPSs and CMSs. That was to say, introducing polyurea in CCSs, either in coating covered or fulfilled states, successfully circumvented the brittleness of CCSs, getting polyurea/CCS interpenetrated composites to perform excellent specific energy-absorbing ability.

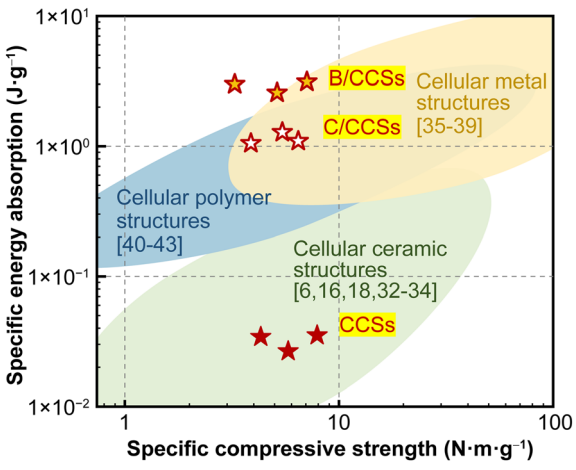

Fig. 10 Ashby map of specific energy absorption versus specific compressive strength

4 Conclusion

Inspired by dual-phase interpenetrated composites in natural materials, CCSs with polyurea were proposed to circumvent the disadvantage effect of CCSs' brittleness. Polyurea coating covered and fulfilled dual-phase interpenetrated composites (C/CCSs and B/CCSs) were

involved. It has been proved that both compressive strength and energy absorption of CCSs increased as the increase in relative density. Catastrophic failure occurred on CCSs under compressive loading. Failure mode of CCSs shifted from localized deformation to fractured entirely because of the increased stiffness. Polyurea gave the polyurea/CCS interpenetrated composites a large deformable ability, making the compression of polyurea/CCS interpenetrated composites go through linear elastic stage, plateau stage, and densification stage. With the help of polyurea coating, C/CCSs maintained their integrity when deformation reached as high as 0.60, avoiding the disintegration of broken fragments. Polyurea coating had less effect on compressive strength of C/CCSs but tremendously improved the energy-absorbing ability from 26.48–52.57 to 1.04–1.89 $MJ{\cdot}m^{-3}$. Furthermore, the failure mode of C/CCSs changed from localized deformation to homogeneous deformation. Fulfilled polyurea provided additional strength and allowed B/CCSs to consume much more energy under compression. So, compressive strength and energy-absorbing ability of B/CCSs were 1.33–1.36 and 2.84–4.61 times those of C/CCSs, respectively. Compared with coating covered C/CCSs, polyurea fulfilled B/CCSs had no advantage in specific load-bearing capacity. But B/CCSs performed well in specific energy-absorbing ability. It was proved that compositing CCSs with polyurea is a reliable way to circumvent the brittleness of CCSs, which could be extensively used in structural components.

Acknowledgements This work was financially supported by the National Natural Science Foundation of China (No. 52275310), the Open Project of State Key Laboratory of Explosion Science and Technology (No. QNKT22-15), and the BIT Research and Innovation Promoting Project (No. 2022YCX020). The authors also want to sincerely thank the characterization at the Analysis & Testing Center, Beijing Institute of Technology

Declarations

Conflict of interests The authors declare that they have no conflict of interest.

References

[1] Wang P, Zhang JZ, Zhang Y, Qin F, Yang MH, Chen HX. Structure and properties of silicon oxycarbide porous ceramics with different catalysts. Chin J Rare Met. 2022;46(12):1573. https://doi.org/10.13373/j.cnki.cjrm.XY21020007.

[2] Zhang XQ, Zhang KQ, Zhang L, Wang WQ, Li Y, He RJ. Additive manufacturing of cellular ceramic structures: from structure to structure-function integration. Mater Des. 2022;215:110470. https://doi.org/10.1016/j.matdes.2022.110470.

[3] Shao CS, Chen LJ, Tang RM, Zhang B, Tang JJ, Ma WN. Degradation and biological performance of porous osteomimetic biphasic calcium phosphate in vitro and in vivo. Rare Met. 2022;41(2):457. https://doi.org/10.1007/s12598-021-01814-0.

[4] Shao CS, Chen LJ, Tang RM, Zhang B, Tang JJ, Ma WN. Polarized hydroxyapatite/$BaTiO_3$ scaffolds with bio-inspired porous structure for enhanced bone penetration. Rare Met. 2022;41(1):67. https://doi.org/10.1007/s12598-021-01798-x.

[5] Sajadi SM, Vásárhelyi L, Mousavi R, Rahmati AH, Kónya Z, Kukovecz Á, Arif T, Filleter T, Vajtai R, Boul P, Pang ZQ, Li T, Tiwary CS, Rahman MM, Ajayan PM. Damage-tolerant 3D-printed ceramics via conformal coating. Sci Adv. 2021;7(28):eabc5028. https://doi.org/10.1126/sciadv.abc5028.

[6] Foratirad H, Maragheh MG, Baharvandi HR. Fabrication of porous titanium carbide ceramics by gelcasting process. Rare Met. 2022;41(9):3220. https://doi.org/10.1007/s12598-018-1068-0.

[7] Yao L, Zhu CC, Jiang JX, Zhou BB. Mechanical properties of Ti_3AlC_2 ceramics before and after heat treatment. Rare Met. 2022;41(8):2777. https://doi.org/10.1007/s12598-015-0609-z.

[8] Liu XY, Zou B, Xing HY, Huang CZ. The preparation of ZrO_2–Al_2O_3 composite ceramic by SLA-3D printing and sintering processing. Ceram Int. 2020;46(1):937. https://doi.org/10.1016/j.ceramint.2019.09.054.

[9] Zhang L, Feih S, Daynes S, Chang S, Wang MY, Wei J, Lu WF. Pseudo-ductile fracture of 3D printed alumina triply periodic minimal surface structures. J Eur Ceram Soc. 2020;40(2):408. https://doi.org/10.1016/j.jeurceramsoc.2019.09.048.

[10] Zhang LZ, Liu H, Yao HH, Zeng Y, Chen JM. 3D printing of hollow lattice structures of $ZrO_2(3Y)$/Al_2O_3 ceramics by vat photopolymerization: process optimization, microstructure evolution and mechanical properties. J Manuf Process. 2022;83:756. https://doi.org/10.1016/j.jmapro.2022.09.047.

[11] Yang T, Jia Z, Chen HS, Deng ZF, Liu WK, Chen LN, Li L. Mechanical design of the highly porous cuttlebone: a bioceramic hard buoyancy tank for cuttlefish. Proc Natl Acad Sci. 2020;117(38):23450. https://doi.org/10.1073/pnas.2009531117.

[12] Ritchie RO. Armoured oyster shells. Nat Mater. 2014;13(5):435. https://doi.org/10.1038/nmat3956.

[13] Barthelat F, Tang H, Zavattieri PD, Li CM, Espinosa HD. On the mechanics of mother-of-pearl: a key feature in the material hierarchical structure. J Mech Phys Solids. 2007;55(2):306. https://doi.org/10.1016/j.jmps.2006.07.007.

[14] Munch E, Launey ME, Alsem DH, Saiz E, Tomsia AP, Ritchie RO. Tough, bio-inspired hybrid materials. Science. 2008;322(5907):1516. https://doi.org/10.1126/science.1164865.

[15] Li M, Zhao NF, Wang MN, Dai XG, Bai H. Conch-shell-inspired tough ceramic. Adv Funct Mater. 2022;32(39):2205309. https://doi.org/10.1002/adfm.202205309.

[16] Zhang XQ, Zhang KQ, Zhang B, Li Y, He RJ. Quasi-static and dynamic mechanical properties of additively manufactured Al_2O_3 ceramic lattice structures: effects of structural configuration. Virtual Phys Prototy. 2022;17(3):528. https://doi.org/10.1080/17452759.2022.2048340.

[17] Lee YH, Lee JW, Yang SY, Lee H, Koh YH, Kim HE. Dual-scale porous biphasic calcium phosphate gyroid scaffolds using ceramic suspensions containing polymer microsphere porogen for digital light processing. Ceram Int. 2021;47(8):11285. https://doi.org/10.1016/j.ceramint.2020.12.254.

[18] Zhang XQ, Zhang KQ, Zhang B, Li Y, He RJ. Additive manufacturing, quasi-static and dynamic compressive behaviours of ceramic lattice structures. J Eur Ceram Soc. 2022;42(15):7102. https://doi.org/10.1016/j.jeurceramsoc.2022.08.018.

[19] Bonatti C, Mohr D. Smooth-shell metamaterials of cubic symmetry: anisotropic elasticity, yield strength and specific energy absorption. Acta Mater. 2019;164:301. https://doi.org/10.1016/j.actamat.2018.10.034.

[20] Markandan K, Lai CQ. Enhanced mechanical properties of 3D printed graphene-polymer composite lattices at very low

graphene concentrations. Compos Part A Appl S. 2020;129:105726. https://doi.org/10.1016/j.compositesa.2019.105726.
[21] Park J, Park K. Compressive behavior of soft lattice structures and their application to functional compliance control. Addit Manuf. 2020;33:101148. https://doi.org/10.1016/j.addma.2020.101148.
[22] Xiao LJ, Feng GZ, Li S, Mu KL, Qin QH, Song WD. Mechanical characterization of additively-manufactured metallic lattice structures with hollow struts under static and dynamic loadings. Int J Impact Eng. 2022;169:104333. https://doi.org/10.1016/j.ijimpeng.2022.104333.
[23] Zhang XQ, Zhang KQ, Zhang B, Li Y, He RJ. Mechanical properties of additively-manufactured cellular ceramic structures: a comprehensive study. J Adv Ceram. 2022;11(12):1918. https://doi.org/10.1007/s40145-022-0656-5.
[24] Seetoh IP, Liu X, Markandan K, Zhen L, Lai CQ. Strength and energy absorption characteristics of Ti6Al4V auxetic 3D anti-tetrachiral metamaterials. Mech Mater. 2021;156:103811. https://doi.org/10.1016/j.mechmat.2021.103811.
[25] Yuan SQ, Chua CK, Zhou K. 3D-printed mechanical metamaterials with high energy absorption. Adv Mater Technol. 2019;4(3):1800419. https://doi.org/10.1002/admt.201800419.
[26] Kolken HMA, Callens SJP, Leeflang MA, Mirzaali MJ, Zadpoor AA. Merging strut-based and minimal surface meta-biomaterials: decoupling surface area from mechanical properties. Addit Manuf. 2022;52:102684. https://doi.org/10.1016/j.addma.2022.102684.
[27] Mora Sierra DC, Heydari Astaraee A, Guagliano M, Bagherifard S. Numerical investigation of Ti6Al4V gradient lattice structures with tailored mechanical response. Adv Eng Mater. 2022;24(4):2101760. https://doi.org/10.1002/adem.202101760.
[28] Niknam H, Akbarzadeh AH. Graded lattice structures: simultaneous enhancement in stiffness and energy absorption. Mater Des. 2020;196:109129. https://doi.org/10.1016/j.matdes.2020.109129.
[29] Zheng HD, Liu LL, Deng CL, Shi ZF, Ning CY. Mechanical properties of AM Ti6Al4V porous scaffolds with various cell structures. Rare Met. 2019;38(6):561. https://doi.org/10.1007/s12598-019-01231-4.
[30] Xue YY, Wang W, Han FS. Enhanced compressive mechanical properties of aluminum based auxetic lattice structures filled with polymers. Compos Part B Eng. 2019;171:183. https://doi.org/10.1016/j.compositesb.2019.05.002.
[31] Al-Ketan O, Soliman A, AlQubaisi AM, Abu Al-Rub RK. Nature-inspired lightweight cellular co-continuous composites with architected periodic gyroidal structures. Adv Eng Mater. 2018;20(2):1700549. https://doi.org/10.1002/adem.201700549.
[32] Shen MH, Qin W, Xing BH, Zhao WM, Gao SY, Sun Y, Jiao T, Zhao Z. Mechanical properties of 3D printed ceramic cellular materials with triply periodic minimal surface architectures. J Eur Ceram Soc. 2021;41(2):1481. https://doi.org/10.1016/j.jeurceramsoc.2020.09.062.
[33] Minasyan T, Liu L, Holovenko Y, Aydinyan S, Hussainova I. Additively manufactured mesostructured $MoSi_2$–Si_3N_4 ceramic lattice. Ceram Int. 2019;45(8):9926. https://doi.org/10.1016/j.ceramint.2019.02.035.
[34] Brodnik NR, Schmidt J, Colombo P, Faber KT. Analysis of multi-scale mechanical properties of ceramic trusses prepared from preceramic polymers. Addit Manuf. 2020;31:100957. https://doi.org/10.1016/j.addma.2019.100957.
[35] Yang L, Yan CZ, Han CJ, Chen P, Yang SF, Shi YS. Mechanical response of a triply periodic minimal surface cellular structures manufactured by selective laser melting. Int J Mech Sci. 2018;148:149. https://doi.org/10.1016/j.ijmecsci.2018.08.039.
[36] Al-Saedi DSJ, Masood SH, Faizan-Ur-Rab M, Alomarah A, Ponnusamy P. Mechanical properties and energy absorption capability of functionally graded F2BCC lattice fabricated by SLM. Mater Des. 2018;144:32. https://doi.org/10.1016/j.matdes.2018.01.059.
[37] Liu YJ, Li SJ, Zhang LC, Hao YL, Sercombe TB. Early plastic deformation behaviour and energy absorption in porous β-type biomedical titanium produced by selective laser melting. Scr Mater. 2018;153:99. https://doi.org/10.1016/j.scriptamat.2018.05.010.
[38] Leary M, Mazur M, Williams H, Yang E, Alghamdi A, Lozanovski B, Zhang X, Shidid D, Farahbod-Sternahl L, Witt G, Kelbassa I, Choong P, Qian M, Brandt M. Inconel 625 lattice structures manufactured by selective laser melting (SLM): mechanical properties, deformation and failure modes. Mater Des. 2018;157:179. https://doi.org/10.1016/j.matdes.2018.06.010.
[39] Dong L. Mechanical response of Ti–6Al–4V hierarchical architected metamaterials. Acta Mater. 2019;175:90. https://doi.org/10.1016/j.actamat.2019.06.004.
[40] Liu WF, Song HW, Huang CG. Maximizing mechanical properties and minimizing support material of PolyJet fabricated 3D lattice structures. Addit Manuf. 2020;35:101257. https://doi.org/10.1016/j.addma.2020.101257.
[41] Ling C, Cernicchi A, Gilchrist MD, Cardiff P. Mechanical behaviour of additively-manufactured polymeric octet-truss lattice structures under quasi-static and dynamic compressive loading. Mater Des. 2019;162:106. https://doi.org/10.1016/j.matdes.2018.11.035.
[42] Keshavarzan M, Kadkhodaei M, Badrossamay M, Karamooz Ravari MR. Investigation on the failure mechanism of triply periodic minimal surface cellular structures fabricated by Vat photopolymerization additive manufacturing under compressive loadings. Mech Mater. 2020;140:103150. https://doi.org/10.1016/j.mechmat.2019.103150.
[43] Jiang H, Ziegler H, Zhang ZN, Meng H, Chronopoulos D, Chen YY. Mechanical properties of 3D printed architected polymer foams under large deformation. Mater Des. 2020;194:108946. https://doi.org/10.1016/j.matdes.2020.108946.